Influence of Iron Salt Anions on Formation and Oxygen Reduction Activity of Fe/N-Doped Mesoporous Carbon Fuel Cell Catalysts

ACS OMEGA

Article

Cite This: ACS Omega 2019, 4, 17662−17671

http://pubs.acs.org/journal/acsodf

Influence of Iron Salt Anions on Formation and Oxygen Reduction Activity of Fe/N-Doped Mesoporous Carbon Fuel Cell Catalysts

Samuel J. Fretz,[†] Caroline Janson,[†] Walter Rosas-Arbelaez, and Anders E. C. Palmqvist*

Department of Chemistry and Chemical Engineering, Chalmers University of Technology, SE-412 96 Göteborg, Sweden

Supporting Information

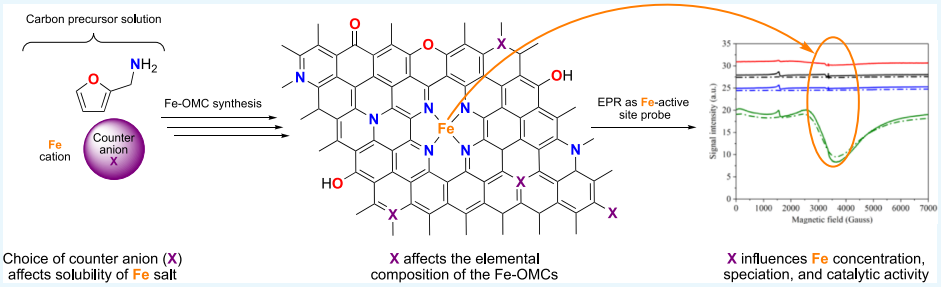

ABSTRACT: Doping carbon materials with transition metal ions can greatly expand their utility, given these metal ions' unique catalytic activity, for example, in oxygen reduction in proton exchange membrane fuel cells. Unlike main group dopants, a counter anion to the metal cation must be selected and this choice has hitherto received little attention for this synthesis method. Herein, we describe the profound effects that the anion has on the resultant iron/nitrogen-doped ordered mesoporous carbons (Fe-OMC). To increase the iron loading and the number of iron-centered catalytically active sites, we selected three iron salts $Fe(OAc)_2$, $Fe(OTf)_2$, and $Fe(BF_4)_2{\cdot}6H_2O$, which show greatly enhanced solubility in the liquid carbon precursor (furfurylamine) compared to $FeCl_3{\cdot}6H_2O$. The increased solubility leads to a significantly higher iron loading in the Fe-OMC prepared with $Fe(OTf)_2$, but the increase in performance as cathode catalysts in fuel cells is only marginal. The Fe-OMCs prepared with $Fe(OAc)_2$ and $Fe(BF_4)_2{\cdot}6H_2O$ exhibited similar or lower iron loadings compared to the Fe-OMC prepared with $FeCl_3{\cdot}6H_2O$ despite their much higher solubilities. Most importantly, the different iron salts affect not only the final iron loading, but also which type of iron species forms in the Fe-OMC with different types showing different catalytic activity.

INTRODUCTION

Carbon materials are prized for their many desirable characteristics including electrical conductivity, porosity, chemical inertness, and low density, allowing them to find applications in supercapacitors, CO_2 capture, batteries, fuel cells, and catalysis among others.[1−4] To increase the utility of carbon materials, different techniques exist to improve their porosity, functionality, and reactivity. One such method is doping, which is the purposeful incorporation of heteroatoms into the carbonaceous structure. This is typically accomplished via a bottom-up method, wherein organic precursors are treated at high temperatures (600−1200 °C) under an inert atmosphere with a template- or structure-directing agent (e.g., mesoporous silica,[5] nanoparticulate $CaCO_3$,[6] eutectic salt mixtures,[7] and phenol−formaldehyde resins[8]). The latter enables formation of a porous and high surface area carbon, while the former determines its dopant elements.[9−11] In the context of an application, the dopant atoms can play just as important of a role as the carbon's porosity.[12] Most studies on doping deal with doping with p-block elements such as nitrogen,[7,13−17] boron,[18−21] phosphorous,[22,23] and sulfur.[12,24,25] For doping with these elements, a wide variety of cheap, abundant carbon precursors are available given these elements' propensity for forming strong, covalent bonds with carbon and their importance in organic chemistry. However, doping carbon materials with transition metal elements requires a different approach. One such method involves the carbonization of preformed metal complexes and macrocycles such as porphyrins,[26−30] phthalocyanines,[31−33] and phenanthroline[34,35] complexes. Disadvantages of this method include the cost of such precursors and their molecular size which may preclude impregnation into the structure-directing agent/template. Another method involves dissolving transition metal salts, directly into a carbon precursor solution.[6,36,37] During the carbon synthesis process, the metal ion is incorporated into the carbon structure along with any codopants, typically nitrogen, which help to form coordinate covalent bonds to the transition metal in the final carbon structure. These metal-centered structures are the active sites for chemical transformations, in particular the oxygen reduction reaction (ORR).[36−39] For iron- and nitrogen-doped ordered mesoporous carbons (OMCs), such sites are designated as $Fe{-}N_x$.

Received: June 18, 2019
Accepted: October 2, 2019
Published: October 16, 2019

Unlike p-block dopants, doping with transition metal salts necessarily involves selecting a counter anion to the cation of the salt. Very few studies exist that systematically explore the effect of the counter anion on the resultant carbon material while using the same metal cation.[40] For metal salts with a multivalent cation and a monovalent anion, doping will involve two or three times the number of anions as cations. In principle, during the heat treatment of the carbon precursor solution, the anion can undergo various processes: it can decompose, form gaseous products, and either react with carbon or leave it largely unaffected (e.g., NO_3^- to NO_x, $C_2O_4^{2-}$ to CO and CO_2); it can carbonize along with the carbon precursor if the anion contains sufficiently high amounts of carbon (e.g., acetate, cyclopentadienyl, and trifluoromethanesulfonate); or, if no decomposition or pyrolysis pathways are available, it can itself be incorporated into the carbon structure thereby adding an extra dopant.

Additionally, the anion can also exert a profound influence on the synthetic process. Within the context of using a lipophilic liquid carbon precursor, the nature of the counter anion determines the solubility of the salt in the carbon precursor solution. It must be stressed that the final metal loading and, in turn, the number of iron active sites of the resultant carbon material is most likely influenced by the solubility of the salt. In our previous studies using furfurylamine as the carbon precursor with KIT-6 silica as the template for the creation of iron- and cobalt-doped OMCs, the dopant salts $FeCl_3{\cdot}6H_2O$ and $CoCl_2$ exhibited relatively limited solubility.[36,37] In this study, we aim to increase the final metal loadings by using alternative iron salts with organic-soluble anions, with the goal to increase the number of $Fe{-}N_x$ active sites for the ORR.

EXPERIMENTAL METHODS

Chemicals and Reagents. The iron salts $FeCl_3{\cdot}6H_2O$ (≥99%), $Fe(OAc)_2$ (≥99.99%), $Fe(OTf)_2$ (≥85%), $Fe(BF_4)_2{\cdot}6H_2O$ (97%), and furfurylamine (≥99%) carbon precursor/solvent were purchased from Sigma-Aldrich and used as received.

Preparation of Saturated Iron Salt Solutions in Furfurylamine. The salts $Fe(OAc)_2$, $Fe(OTf)_2$, and $Fe(BF_4)_2{\cdot}6H_2O$ show exothermic dissolution in furfurylamine so care must be taken so as to not prepolymerize the furfurylamine solvent. Furfurylamine (3 mL) was transferred to a 10 mL centrifuge tube and was cooled to 0 °C in an ice-water bath with a small magnetic stir bar. The iron salt was added in small portions (50−100 mg) while stirring the solution at 0 °C. Enough salt was added such that small amounts of the undissolved solid could be observed at the bottom of the tube. The ice bath was removed, and the solution was allowed to warm to RT. The solution was sonicated for 3 min to ensure complete dissolution of the iron salt and was then centrifuged for 1 min at 5600 rpm. If no solid was observed at the bottom of the tube, the solution was re-cooled to 0 °C and more salt was added. The process was repeated until saturation was reached and solid salt was observed at RT. Fresh iron salt solutions were prepared for each impregnation.

Synthesis of Fe-Doped OMCs. Mesoporous silica (KIT-6) was prepared according to a published procedure[5] and was used as a template for all mesoporous carbon catalysts. All samples were prepared from the same batch of KIT-6. The KIT-6 template was dried at 150 °C overnight (16 h) before use. Into a 60 mL quartz crucible (Saveen Werner) was placed 2 g of dried KIT-6. Silica was allowed to cool to room temperature and a volume of the dissolved iron salt in furfurylamine was added to the silica. The volume added corresponded to the pore volume of the silica (2 mL). The slurry was thoroughly mixed to ensure complete pore filling. After mixing, the impregnated silica was a homogeneous brown color and was gently pressed into a single piece in the bottom of the crucible. The top of the crucible was covered with parafilm and then a quartz crucible lid. All crucibles were placed in a Styrofoam box overnight (16 h) to allow for complete impregnation of the silica in the absence of light. The crucibles were taken out from the box and the lid and parafilm removed. The crucibles were covered tightly with aluminum foil and heated in an air oven at 100 °C for 2 h then at 160 °C for 2 additional hours to polymerize furfurylamine. The black silica−polymer composite was transferred to a 40 mL aluminum crucible (Almath) and heated at a rate of 15 °C min^{-1} to 950 °C, where it was carbonized for 4 h. All samples were carbonized individually. The carbon−silica composites were ball milled for 30 min at 15 Hz using a Retsch MM400 ball mill with a 25 mL ZrO_2-coated cup and a 15 mm diameter ZrO_2 ball. Thereafter, nitrogen sorption was performed on the carbon−silica composite to determine the residual pore volume. The previous process of impregnation, polymerization, and pyrolysis was repeated once more with the once-filled carbon−silica composites. The only change to this procedure for the second round was the volume of iron salt solution in furfurylamine added to the carbon−silica composite corresponded to the residual pore volume, and the sample was pyrolyzed for 6 h at 950 °C. The silica template was removed by acid washing with 40 wt % HF in H_2O at room temperature followed by stirring in distilled water for 24 h at RT. A postsynthetic acidic treatment was performed by heating the OMC in an aqueous 0.5 M H_2SO_4 for 6 h at 80 °C followed by filtering and washing with distilled water before a final pyrolysis at 950 °C for 2 h. Finally, the samples were once more ball milled but now for 1 h each at 15 Hz before characterization.

Instrumental Techniques. Powder X-ray diffractograms were recorded on all samples using a Bruker D8 ADVANCE and Cu Kα radiation (λ = 0.1542 nm). The 2θ range covered was 10°−80° with a step size of 0.025° and a dwell time at each point of 3 s. Thermogravimetric analysis (TGA) was performed on approximately 10 mg of OMC in a 50 μL alumina crucible in air. The temperature was increased at a rate of 25 °C min^{-1} to 900 °C, where it was kept for 20 min. For the orange powder residue created from the TGA of a sample of OTf-Fe-OMC, a "zero height" X-ray diffraction (XRD) holder was used. Surface area, pore volume, and pore size distribution were measured by nitrogen sorption using a TriStar 3000 instrument from Micromeritics. All samples were degassed for a minimum of 3 h at 200 °C under a nitrogen flow. The surface areas and pore volumes were calculated using the Brunauer−Emmett−Teller (BET) and Barrett−Joyner−Halenda (BJH) algorithms, respectively, on the adsorption isotherm. Elemental analysis (EA) was performed on an Elementar Vario MICRO Cube HCNS analyzer on approximately 2 mg of sample. X-ray fluorescence (XRF) was conducted on a Philips MagiX PW2424 X-ray spectrometer equipped with a Rh tube instrument. About 50 mg of Fe-OMC was evenly distributed between two polypropylene films in the sample holder. The measured data was evaluated using the UniQuant and IQ+ applications. Small-angle X-ray scattering

DOI: 10.1021/acsomega.9b01803
ACS Omega 2019, 4, 17662−17671

(SAXS) experiments were carried out using a Mat:Nordic instrument from SAXSLAB. The setup used was equipped with a Rigaku high brilliance microfocus X-ray source with Cu Kα radiation. The sample was placed in an evacuated sample chamber and the entire space between the collimator and detector was evacuated to minimize air scattering. A Pilatus 300K detector was used to record the scattering intensity. The sample-to-detector distance was about 1580 mm as obtained from a calibration of the scattering angle 2θ using silver behenate as a reference. A sandwich cell holder was used for the carbon powders. X-band electron paramagnetic resonance (EPR) spectroscopy measurements were conducted on powder samples (10 mg) in quartz tubes using a Bruker ELEXSYS E500 EPR. The modulation power was 6.345 mW and the modulation amplitude 5G.

Rotating Disk Electrode Measurements. Rotating disk electrode (RDE) measurements were carried out using a three-electrode instrument (Gamry Instruments) at room temperature. A graphite-rod (6 mm-diameter) counter electrode and $Ag/AgCl_{sat}$ reference electrode were used. All potentials reported in this study were converted to the reversible hydrogen electrode (RHE). A glassy carbon (diameter: 5.0 mm) RDE was used as the working electrode. This electrode was polished with a 1.0 μm diamond suspension and then with a 0.5 μm alumina suspension followed by copious washing with water and ethanol in order to give it a mirror-like finish. Catalyst inks were prepared by mixing 10 mg of the Fe-OMC catalyst with 95 μL of Nafion solution (5 wt % in lower aliphatic alcohols and water, Sigma-Aldrich) and 350 μL of absolute ethanol (VWR). After sonication for 30 min assuring a homogenous dispersion, a 5 μL ink aliquot was drop-coated onto the well-polished glassy carbon electrode and dried at ambient conditions for 30 min. The resulting catalyst loading for all cases was 580 $\mu g\ cm^{-2}$. A steady-state program was run on all catalysts in 0.1 M $HClO_4$ and 0.1 M KOH both bubbled with oxygen until saturation at four different rotation speeds: 100, 400, 900, and 1600 rpm. The program started at 1 V versus RHE and decreased in steps of 30 mV with a holding time of 60 s, down to 0 V versus RHE.

Screen Printing of the Cathode Electrode and Preparation of the MEA. In the preparation of the fuel cell cathode electrode ink, 0.2 g of propylene glycol (99% Sigma-Aldrich), 1.65 g Nafion D2021 solution (Fuel cell store), and 1 drop (about 0.02 g) of dispersant KD2, were mixed in a vial. Thereafter, 0.5 g of the Fe-OMC catalyst powder was added and mixed with an Ultrathurrax (Heidolph, Silent Crusher M) for about 2 min, followed by the addition of 0.13 g Vulcan XC-72R (Fuel Cell Store) and once again mixing with an Ultrathurrax for about 2 min. The inks were screen printed with a Dyenamo DN-HM02 Laboratory screen-printer on Toray Paper TGP-H-060 (Fuel Cell Earth) as squares with an area of 2.56 cm^2. The printed catalysts were dried and then washed carefully in deionized water to remove propylene glycol. The catalyst loading was about 1.6 mg cm^{-2}. A commercial Pt/C catalyst (10 wt % Pt/Vulcan with 0.5 mg Pt cm^{-2} from Quintech) was used at the anode side. To complete the membrane electrode assembly (MEA) a commercial ionomer, Nafion Membrane NM-212 (Quintech), was used. Detailed parameters for the MEA preparation are given in the cited reference.[41]

Proton Exchange Membrane Fuel Cell Measurements. The PEM fuel cell tests of the prepared catalyst materials were done in a single cell fuel cell, using a commercial 5 cm^2 polymer electrolyte membrane fuel cell (PEMFC) from Scribner Assoc. with an effective electrode area of 2.56 cm^2. All measurements were done at 80 °C. The cell was fueled with fully humidified 100% H_2 (instrumental grade from AGA) and using synthetic air (instrumental grade from AGA) as a fully humidified oxidant. A back pressure of 1.5 bar was applied at both the anode and cathode side of the cell.

RESULTS AND DISCUSSION

The main goal of this study was to increase the iron content of the final Fe-OMC by using more organic soluble salts, which, in turn, should hopefully increase the Fe-OMCs' catalytic activity toward the ORR. We selected iron(II) tetrafluoroborate hexahydrate, $Fe(BF_4)_2{\cdot}6H_2O$, and iron(II) trifluoromethanesulfonate, $Fe(OTf)_2$, as lipophilic salts with weakly coordinating anions, which should allow for increased coordination between the amine groups and iron cations. We also selected iron(II) acetate, $Fe(OAc)_2$, as a salt with increased solubility with an organic anion. Unlike the other three salts investigated, the acetate anion in $Fe(OAc)_2$ does not add any additional elements to the precursor mixture. Iron(III) chloride hexahydrate, $FeCl_3{\cdot}6H_2O$, was used as the reference dopant.[42] The Fe-OMCs are designated by their anion; for example, the Fe-OMC prepared using $FeCl_3{\cdot}6H_2O$ as the dopant salt is referenced as Cl-Fe-OMC. References to the salt itself use the full name.

As expected, the salts $Fe(OAc)_2$, $Fe(OTf)_2$, and $Fe(BF_4)_2{\cdot}6H_2O$ are significantly more soluble in the furfurylamine solvent than the standard $FeCl_3{\cdot}6H_2O$ (about 5−7 times more, see Table 1). These solutions in furfurylamine are nearly black

Table 1. Relative Solubility of Iron Salts in Furfurylamine

	approximate saturation limit		
iron salt	g L^{-1}	mol L^{-1}	Fe/furfurylamine molar ratio
$Fe(OAc)_2$	300	1.72	1:6
$FeCl_3{\cdot}6H_2O$	60	0.22	1:43
$Fe(BF_4)_2{\cdot}6H_2O$	430	1.27	1:7
$Fe(OTf)_2$	440	1.24	1:8

in color whereas $FeCl_3{\cdot}6H_2O$ is only slightly brown. The potential for strong exotherms upon dissolution causing premature polymerization of the furfurylamine solvent also proved troublesome, which is why all mixing was performed at 0 °C. The higher viscosities of these solutions required extending the template-impregnation times (16 h) to ensure efficient pore filling. After template removal with HF, the Fe-OMCs were subjected to a sulfuric acid washing step followed by an additional carbonization to remove any undesirable iron species that are not bound or coordinated to the nitrogen-modified carbon matrix. This treatment has previously been found to improve the ORR performance of Fe-OMCs in PEMFCs.[36]

Elemental Compositions. To determine the elemental compositions and to assess if the iron content was indeed increased in the final Fe-OMC catalysts, we performed EA, XRF, and TGA on the prepared Fe-OMCs. EA quantifies the amounts of hydrogen, carbon, nitrogen, and sulfur present by analyzing the gases after combustion while XRF measures the iron content. The TGA, which was ran to 900 °C in air, determines the H_2O content (hydration weight) and the residual mass after combustion. All iron was assumed to be

DOI: 10.1021/acsomega.9b01803
ACS Omega 2019, 4, 17662−17671

Table 2. Elemental and Thermogravimetric Analysis for Fe-OMCs[a]

sample	H_2O[b] (hydration)	H[c]	C[c]	N[c]	S[c]	Fe[d]	other non-volatiles[b,d]	other volatiles
OAc-Fe-OMC	0.45	0.58	93.21	0.92	0.20	0.11	0.21	4.64
Cl-Fe-OMC	3.22	1.00	83.42	3.68	0.11	0.40	0.52	7.65
BF_4-Fe-OMC	3.03	0.71	85.83	4.23	0.27	0.46	3.52	1.95
OTf-Fe-OMC	2.31	1.08	79.97	3.05	2.73	3.88	0.78	6.20

[a]All units are weight percent (wt %). [b]Determined by TGA. [c]Determined by EA. [d]Determined by XRF.

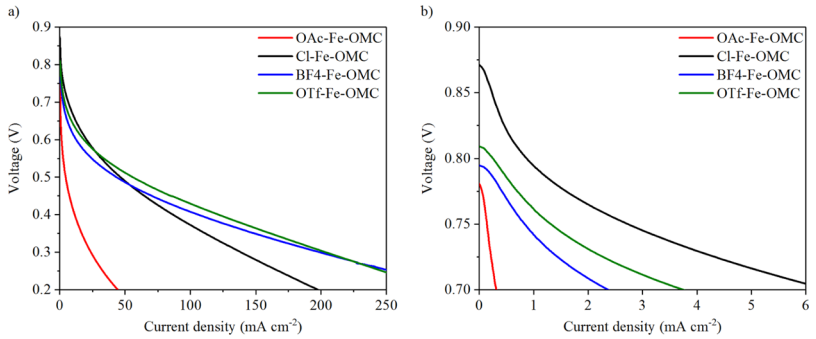

Figure 1. (a) Polarization curves and (b) zoom in of low current density regions measured in a single cell PEM fuel cell for Fe-OMCs. Measured at 80 °C, 100% relative humidity, 1.5 bar backpressure on both electrodes, H_2 (100%) flow rate 100 mL min^{-1}, air flow rate 200 mL min^{-1}, Nafion membrane NRE-212 used, Fe-OMC loading on the cathode GDLs was about 1.6 mg/cm^2.

part of the residual mass and the difference between these two was assumed to be other nonvolatile elements (e.g., B). The difference between all seven masses and 100 wt % was assumed to be nondetectible volatile elements (e.g., O, F, and Cl). The results for all three methods are summarized in Table 2 and the details are given in the Supporting Information. EA reveals a large nitrogen content in Cl-Fe-OMC, OTf-Fe-OMC, and BF_4-Fe-OMC, indicating that the nitrogen functionality from the furfurylamine carbon precursor was successfully incorporated into the carbon structure; the nitrogen content should allow for ligating atoms to iron cations to form Fe−N_x chelates. OAc-Fe-OMC, however, exhibits a markedly lower nitrogen content, which also correlates with measurably lower hydration content, likely indicating a more hydrophobic carbon. All samples show some sulfur content, perhaps due to the postsynthesis treatment with sulfuric acid. OTf-Fe-OMC displays a much higher sulfur content of a few wt %. This is likely due to the sulfur atoms in the trifluoromethanesulfonate counter anion; this anion carbonizes along with the furfurylamine precursor.

The XRF results demonstrate that all samples prepared contain iron. Comparing the order of solubilities of the salts with the resulting iron contents in the formed Fe-OMCs, it is clear that iron incorporation is not directly related to the solubility of the salts alone. This is exemplified in the case of $Fe(OAc)_2$ in that its solubility is ca. 5 fold greater than $FeCl_3 \cdot 6H_2O$, but generates the lowest iron loading for its respective Fe-OMC at ca. 0.11 wt %, or about one-fourth the iron loading for Cl-Fe-OMC. The lower iron loading of OAc-Fe-OMC correlates with its low nitrogen content, suggesting that the iron loading is limited by the number of ligating atoms to form Fe−N_x chelates. The iron and nitrogen loadings of BF_4-Fe-OMC is quite similar to Cl-Fe-OMC, but its other nonvolatile mass is considerably larger than the other three Fe-OMCs, which could be due to boron- and/or fluorine-containing species formed from the BF_4^- anions. The amorphous, brown state of the residue from the TGA burn-off is consistent with this assignment. This residue, unfortunately, adhered too strongly to the crucible for further analysis. The iron loading for OTf-Fe-OMC is much higher than the other three at nearly 4 wt %, which suggests that some soluble iron salts can indeed increase the final iron loading. The nitrogen loading of OTf-Fe-OMC is, however, lower than the Cl-Fe-OMC, whereas the sulfur content is very high, suggesting that the iron in OTf-Fe-OMC is, at least partly, associated with sulfur as $Fe_{1-x}S$ (see Figure 3d). Interestingly, the combustion of OTf-Fe-OMC in TGA resulted in an orange-red powder, which was amenable for XRD analysis (XRD, Figure S2). The X-ray diffractogram is consistent with Fe_2O_3, which is to be expected to form from oxidation of $Fe_{1-x}S$ at 900 °C. The mass of the TGA-combusted sample together with its known chemical identity allows for another method of determining the iron content of this Fe-OMC, which was calculated to be 3.26 wt %. This value is slightly lower than the 3.88 wt % as determined by XRF but is still appreciably higher than the other three Fe-OMCs. Overall, these results indicated that the nature of the counter anion exerts a profound influence on the final iron loading and on the type of iron species formed in the Fe-OMC.

Evaluation of Fe-OMCs as Fuel Cell Cathode Catalysts. The Fe-OMC's catalytic activity was evaluated in a single cell PEMFC. The polarization plots of the four samples are shown in Figure 1. In the kinetically controlled region (low current densities), Cl-Fe-OMC performs best with the highest voltage, indicating that this catalyst has the highest activity toward the ORR. At higher current densities, OTf-Fe-OMC and BF_4-Fe-OMC outperform Cl-Fe-OMC, which suggests better mass transport in these Fe-OMCs. In the power plots (Figure S3), OTf-Fe-OMC and BF_4-Fe-OMC provide slightly higher maximum power outputs compared to Cl-Fe-OMC. The relatively low activity values obtained for all samples are similar to those reported earlier for Cl-Fe-OMC samples prepared under similar conditions with a pyrolysis temperature of 950 °C.[43] The OAc-Fe-OMC sample shows the highest overpotential and the worst performance over all current densities studied. Such low performance is indicative of a low number of ORR active sites, which correlates well to its low

DOI: 10.1021/acsomega.9b01803
ACS Omega 2019, 4, 17662−17671

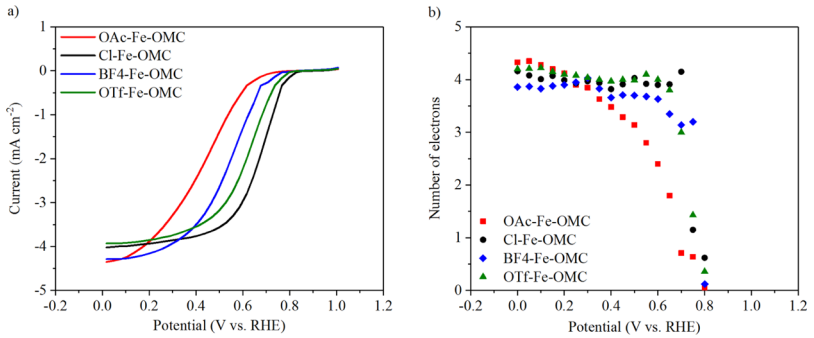

Figure 2. (a) RDE polarization plots collected in the O_2-saturated 0.1 M $HClO_4$ electrolyte at 10 mV s^{-1} with a rotation rate of 900 rpm at room temperature and (b) number of electrons transferred for the Fe-OMC catalysts as determined by the Koutecky–Levich equation. At potentials greater than 0.8 V, the number of electrons transferred was determined to be zero for all Fe-OMC catalysts.

iron and nitrogen loadings because these elements are strongly associated with the active site itself and/or its formation.[36−38]

Despite its higher iron content, OTf-Fe-OMC does not exhibit correspondingly better performance in the PEMFC. To further elucidate the mechanism of O_2 reduction, we studied the Fe-OMCs on RDEs. The Fe-OMCs were first studied in 0.1 M $HClO_4$ to approximate the acidic polymer electrolyte of the PEMFCs, albeit at 25 °C instead of 80 °C (Figure 2a). Cl-Fe-OMC shows the highest half-wave potential ($E_{1/2}$) at 0.68 V versus RHE with OTf-Fe-OMC and BF_4-Fe-OMC closely behind at 0.62 and 0.56 V, respectively. OAc-Fe-OMC performed much worse, exhibiting a high overpotential and an $E_{1/2}$ of 0.44 V. These results corroborate those found in PEMFCs, where the better performance of Cl-Fe-OMC at lower current densities could be attributed to a lower overpotential in acidic media. We also applied the Koutecky–Levich equation to the electrode current densities at different rotating rates in order to determine the number of transferred electrons per O_2 molecule as a function of applied potential (Figures 1b, S4, and S7, left; details in the Supporting Information). Based on this calculation, Cl-Fe-OMC follows a four-electron reduction mechanism over all potentials up to 0.7 V. OTf-Fe-OMC and BF_4-Fe-OMC also follow a four-electron transfer mechanism, except at higher potentials (less overpotential) where this number drops to about three at 0.7 V. This, too, corroborates the PEMFC results in that Cl-Fe-OMC performs best at higher potentials (lower current densities) but this difference is partly negated at lower potentials (higher current densities) where additional aspects of electrode resistance and mass transport become increasingly important. In contrast, the mechanism of the OAc-Fe-OMC follows a much different trend. At low potentials, it follows a four-electron mechanism and this number is reduced to less than one at higher potentials, leading to an incomplete ORR and the formation of H_2O_2 and/or other partially reduced oxygen species. This trend matches well to the poor performance of this catalyst in PEMFC and its lower nitrogen and iron content.

An additional ORR study was carried out in 0.1 M KOH solution saturated with oxygen (Figure S5a). In this case, we observed a better performance compared to 0.1 M $HClO_4$ for all four Fe-OMCs in terms of the $E_{1/2}$ and number of electrons transferred. The OTf-Fe-OMC is slightly better than the other Fe-OMCs with an $E_{1/2}$ of 0.86 V. The Cl-Fe-OMC and BF_4-Fe-OMC demonstrate very similar $E_{1/2}$ of 0.845 V while the OAc-Fe-OMC, as before, performs the worst with an $E_{1/2}$ of 0.78 V. The number of electrons transferred is roughly four at lower potentials until 0.7 V, at which point the number decreases consistently for all catalysts with the OAc-Fe-OMC catalyst exhibiting the lowest number at each potential between 0.7 and 0.9 V (Figures S5b, S6, and S7, right). The improved performance for all Fe-OMCs can be attributed to the reduced adsorption energies of anions in the alkaline environment, specifically of the hydrogen peroxide intermediate (HO_2^-), which reduces overpotentials for further electron transfer.[44,45] However, we could again confirm that OAc-Fe-OMC has the poorest performance among the four Fe-OMCs.

Further Characterization of Fe-OMCs. The textural nature of the OMCs also has an impact on the catalyst performance, so it was investigated by nitrogen sorption, SAXS and XRD. The nitrogen isotherms show that the nature of the iron salt has a strong influence on the surface area and pore structure (Table 3 and Figure 3a). While all samples had

Table 3. Surface Properties of the Fe-Doped OMCs

sample	BET surface area (m^2 g^{-1})	BJH pore volume (cm^3 g^{-1})[a]	pore diameter maximum (Å)[a]
OAc-Fe-OMC	607	1.26	25
Cl-Fe-OMC	1035	1.29	41
BF_4-Fe-OMC	572	1.19	60
OTf-Fe-OMC	709	1.02	52

[a]Based on the adsorption isotherm.

similar BJH pore volumes, the surface area of Cl-Fe-OMC is considerably higher than the other three, by about a factor of two. The higher surface area could enhance the catalytic activity of this OMC in PEMFCs by supplying a higher number of active sites on the surface. While all four OMCs yield distorted type IV isotherms, only Cl-Fe-OMC, OTf-Fe-OMC, and BF_4-Fe-OMC show a steep rise over small pressure changes indicative of well-defined pore diameters. Indeed, Figure 3b reveals that these Fe-OMCs have relatively narrow pore size distributions with relatively sharp maxima around 41, 52, and 60 Å, respectively. OAc-Fe-OMC exhibits an isotherm indicative of a partly macroporous material and a much broader pore diameter distribution with a shallow maximum around 25 Å. The larger pore diameters of OTf-Fe-OMC and BF_4-Fe-OMC could explain their enhanced performance in PEMFCs at higher current densities where mass transport of the water exhaust becomes the limiting factor.

The SAXS patterns corroborate these differences in the pore structure (Figure 3c). We observe that Cl-Fe-OMC, OTf-Fe-OMC, and BF_4-Fe-OMC exhibit mesostructured pore systems

DOI: 10.1021/acsomega.9b01803
ACS Omega 2019, 4, 17662−17671

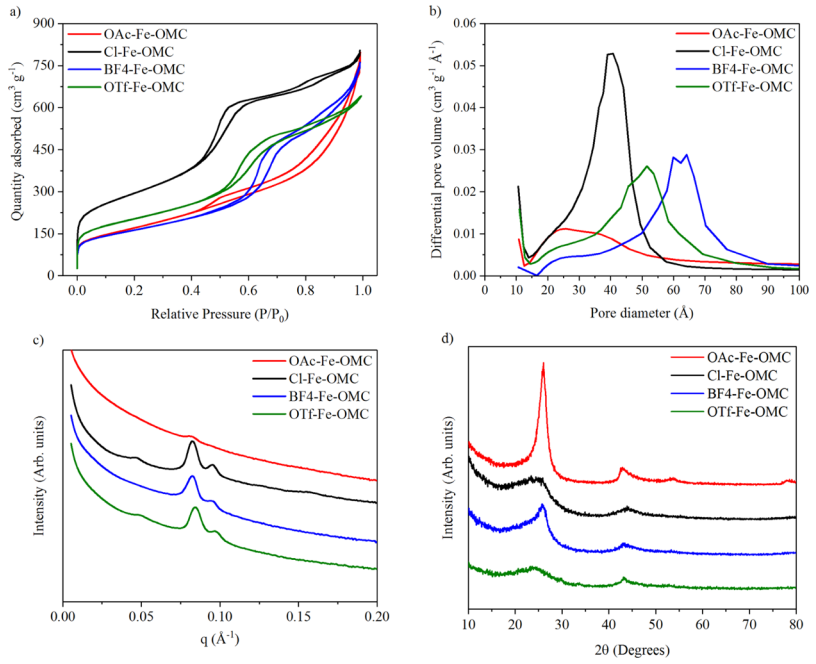

Figure 3. (a) Nitrogen isotherms, (b) pore diameter distributions based on the adsorption isotherm, (c) SAXS plots (SAXS), and (d) X-ray diffractograms for Fe-OMCs. In the SAXS and XRD plots, the traces have been offset in intensity for clarity.

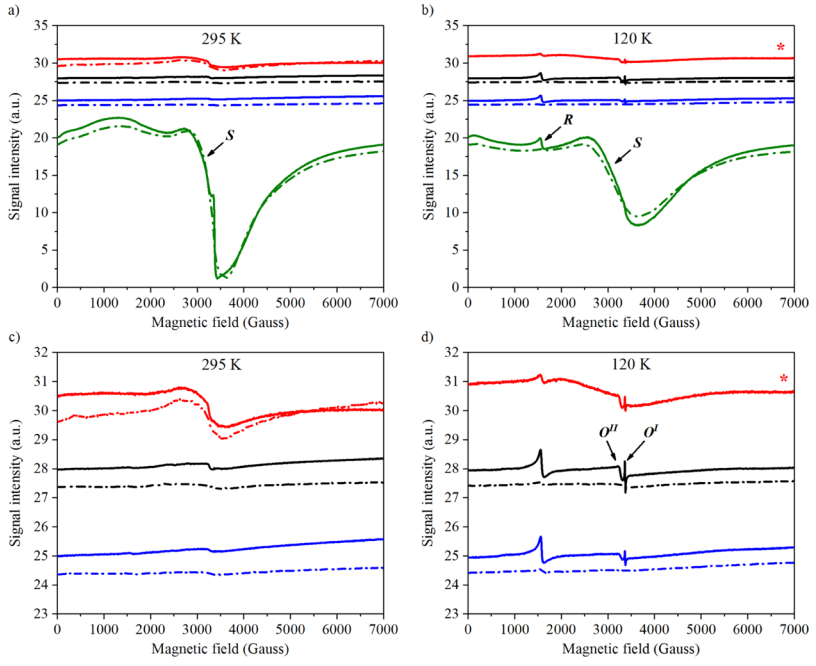

Figure 4. (a) EPR spectra measured at 295 K, (b) EPR spectra at 120 K, (c) zoom in of the spectra at 295 K, and (d) zoom-in of spectra at 120 K for OAc-Fe-OMC (red), Cl-Fe-OMC (black), BF_4-Fe-OMC (blue), and OTf-Fe-OMC (green). Spectra were taken either in air (solid line) or a nitrogen atmosphere (dotted line). The traces have been offset in intensity for clarity. *Sample OAc-Fe-OMC was not amenable for analysis in a nitrogen atmosphere at 120 K.

that are negative replicas of the KIT-6 silica template, which gives a cubic *Ia3d* structure, with the typical (211) and (220) reflections.[5] The lattice constants of Cl-Fe-OMC, OTf-Fe-OMC, and BF_4-Fe-OMC are similar with values of 18.8, 18.7, and 18.3 nm, respectively, which confirm the typical lattice sizes of such a cubic structure formed in OMCs using KIT-6 as a template. However, OAc-Fe-OMC diffracts only weakly indicating a lack of periodicity in the mesoscale and a poorly defined pore structure. This lack of a mesostructure adds another reason to explain the poor performance of this OMC in electrochemical testing; its disordered pore system could impede mass transport to the active sites, thereby attenuating its efficiency in the ORR.

XRD can yield valuable information on the atomic structure of the Fe-OMCs; it reveals the degree of graphitization of Fe-OMC and if crystalline metal or metal oxide nanoparticles are present. All four diffractograms (Figure 3d) show the expected peaks at 2θ values of 26° and 43°, corresponding to the

DOI: 10.1021/acsomega.9b01803
ACS Omega 2019, 4, 17662−17671

reflections (002) and (101) of amorphous carbon.[11] However, their intensity differs markedly: OAc-Fe-OMC shows much sharper and intense peaks at these angles in addition to two more at 54° and 78°, indicating a higher level of graphitization compared to the other Fe-OMCs. The carbonizable acetate anion in $Fe(OAc)_2$ likely helps the graphitization process and the high concentration of iron ions could catalyze it. Because graphitization is known to remove heteroatoms from the carbon structure, the low iron and nitrogen loadings and high carbon content in OAc-Fe-OMC is consistent with its more graphitic structure.[11] BF_4-Fe-OMC exhibits a more graphitic structure as well, although less so than OAc-Fe-OMC. Two very weak diffraction peaks for OTf-Fe-OMC were observed between 30° and 35°, suggesting the presence of some crystalline particles in the OTf-Fe-OMC sample such as $Fe_{1-x}S$.[43] No sharp diffraction peaks were observed for any of the other Fe-OMCs, signifying low amounts or the complete absence of iron or iron oxide/sulfide particles.

Probing the Active Site: Electron Paramagnetic Resonance. To gain insight into the nature of the active sites, we characterized the Fe-OMCs with EPR spectroscopy. Using this technique, species with unpaired electrons such as radicals and many transition metal ions are detectable. Unpaired electrons occur in iron species depending on its spin and oxidation states including Fe(III) and high-spin Fe(II) species. For a Fe-centered active site with activity toward the ORR, its spin and oxidation states are expected to be influenced by its interaction with O_2. To study such Fe−O_2 interactions, the catalyst powders were, prior to the EPR-measurements, flushed with either nitrogen or air atmospheres. Furthermore, the experiments were performed at two different temperatures (295 and 120 K) because many EPR signals are temperature dependent. In a detailed EPR study, we have learned that changing the atmosphere and/or temperature among measurements enables the origin of the EPR signals from Fe-OMCs.[46] In the present study, EPR was mainly used to determine the presence or absence of iron in the Fe-OMC catalysts and to identify possible differences in types of iron species present in the different samples.

As shown in Figure 4, EPR-signals were observed in all Fe-OMCs. The signals are consistent with the presence of paramagnetic iron species and confirm coordination of iron within the OMC structure.[46] However, panels (a and b) show clear differences in the EPR-signals for the four synthesized Fe-OMCs, which confirms that the different iron salts strongly impact the catalysts' final iron coordination and the formation of different iron species during the synthesis.

In general, the EPR-spectra of the BF_4-Fe-OMC and Cl-Fe-OMC look rather similar, which may simply indicate that the use of the two iron salts ($Fe(BF_4)_2{\cdot}6H_2O$ and $FeCl_3{\cdot}6H_2O$) results in similar types of Fe-OMCs regarding the iron coordination. Although, it should be mentioned that low-spin iron(II) species are EPR-silent and therefore undetectable with EPR. Accordingly, despite the considerably higher solubility of $Fe(BF_4)_2{\cdot}6H_2O$ compared to $FeCl_3{\cdot}6H_2O$ in the carbon precursor solution, the iron-coordination in the final catalyst ends up being similar from an EPR perspective. The similar iron loadings and electrochemical performance of these Fe-OMCs corroborate this hypothesis. The large concentration of other nonvolatile elements in BF_4-Fe-OMC (Table 2), which is likely boron and/or fluorine species produced from the BF_4^- anions, appear not to have a significant influence on the iron coordination or catalytic activity. In the case of these two Fe-OMCs, the small electrochemical differences between them may rather relate to the carbon structure, as has been shown in XRD and nitrogen sorption (Figure 3).

By studying the EPR-spectra measured in air at 120 K (Figure 4d), a signal around 1500 G (g = 4.25) denoted **R**, a sharp signal around ∼3400 G (g = ∼2.00) denoted $\mathbf{O^I}$, and a signal around ∼3200 G (g = ∼2.07) denoted $\mathbf{O^{II}}$, could be observed.[45] The **R** signal appears in all materials studied, although the amplitude of the signal in OAc-Fe-OMC is considerably lower. This signal is typically attributed to high spin iron(III) in a rhombic structure.[45,47−49] The reduction in signal amplitude is noticeable when the Fe-OMC is flushed with nitrogen. We hypothesize that this change in the signal is associated with an iron(II) species that is not detectable or EPR-silent under nitrogen exposure, which is partly oxidized to a paramagnetic iron(III) species (in air) by iron interaction with oxygen.[46] The $\mathbf{O^I}$ and $\mathbf{O^{II}}$ signals are assigned to an oxygen radical (possibly superoxide) which is formed when dioxygen oxidizes iron(II) species into iron(III).[50,51] We suggest that the identified iron species giving rise to the **R**, $\mathbf{O^I}$, and $\mathbf{O^{II}}$ signals are related to the ORR active sites, although this is not yet unambiguously confirmed.[46]

The most deviating EPR spectrum was obtained for the OTf-Fe-OMC (green trace), which exhibits a broad, amplitude intense signal between 2500 and 3500 G (Figure 4a,b, denoted **S**). Interestingly, the amplitude of the **S** signal significantly decreases when the temperature is decreased from 295 to 120 K but its amplitude seems to be unaffected by a change of atmosphere. The **S** signal, with its temperature-dependent behavior, is typically assigned to superparamagnetic particles.[52,53] The superparamagnetic particles in OTf-Fe-OMC are consistent with the presence of $Fe_{1-x}S$[54−56] and/or Fe_2O_3,[52,53] consistent both with the weak diffraction peaks in XRD (Figure 3d) and the XRD of the combusted OTf-Fe-OMC sample (Figure S2). An **S** signal is also observed in OAc-Fe-OMC, although with a lower signal amplitude indicating a lower concentration of superparamagnetic species. In the BF_4-Fe-OMC and Cl-Fe-OMC catalysts, no **S** signal was detectable, suggesting negligible amounts of superparamagnetic particles in these samples. Given the similar performance of Cl-Fe-OMC, BF_4-Fe-OMC, and OTf-Fe-OMC in the RDE and fuel cell tests and the much higher iron loading obtained for OTf-Fe-OMC relative to the other two, we suggest that the iron species giving rise to the **S** signal is not related to any ORR activity. However, some amount of active iron species must be present in the OTf-Fe-OMC based on its performance in the fuel cell test; its $\mathbf{O^I}$ and $\mathbf{O^{II}}$ signals are, however, missing and could be obscured by the large **S** signal.

To summarize the EPR results, we can conclude that the use of different iron salts definitively influences the formation of different iron species in the Fe-OMC catalysts. The different solubilities of the iron salts in the carbon precursor may not necessarily increase the iron loading in the Fe-OMCs or their performance in PEMFCs, but it does influence the type of iron species formed. Of the identified iron in the Fe-OMCs, some iron species are related to the ORR active sites, whereas parts of the iron appear as superparamagnetic particles ($Fe_{1-x}S$ and/or Fe_2O_3) that are most plausibly inactive.

CONCLUSIONS

Overall, these findings signify that the nature of the iron salt used in the carbon synthesis has a profound influence on the structure, chemical composition, and catalytic activity of the

DOI: 10.1021/acsomega.9b01803
ACS Omega 2019, 4, 17662−17671

resultant iron/nitrogen-doped OMCs (Fe-OMC). By changing the anion from chloride (Cl^-) to one more soluble in organic media, acetate (OAc^-), trifluoromethanesulfonate (OTf^-), or tetrafluoroborate (BF_4^-), the amount of salt in the furfuryl-amine precursor solution can be dramatically increased by a factor of 5−7. This enhanced solubility, in the case of OTf^-, leads to significantly higher iron loadings in OTf-Fe-OMC compared to Cl-Fe-OMC. However, the higher solubility of BF_4^- produces an Fe-OMC with a similar iron loading to the standard chloride salt, but with a much higher concentration of other nonvolatile elements, which was likely formed from the BF_4^- counter anions. Moreover, the EPR results indicate very similar iron species contained within BF_4-Fe-OMC and Cl-Fe-OMC. In the case of OAc-Fe-OMC, however, its final iron and nitrogen contents were lower than for Cl-Fe-OMC, confirming the need for incorporation of chelating heteroatoms such as nitrogen in the carbon structure to coordinate the iron atoms.[39] Most importantly, however, the increased solubility of these salts did not produce Fe-OMCs with noticeably better catalytic performance in the ORR in PEMFCs. Because Cl-Fe-OMC, OTf-Fe-OMC, and BF_4-Fe-OMC perform similarly, we conclude that the different salts exhibit different selectivities for the formation of ORR active sites; the additional iron in OTf-Fe-OMC over Cl-Fe-OMC and BF_4-Fe-OMC is apparently ORR inactive.

Nevertheless, these results highlight an opportunity for increasing the catalytic efficiency of iron-doped carbon materials. By changing certain synthesis conditions, e.g., the carbonization temperature, iron salt concentration, carbon precursor, or level of nitrogen doping, the efficiency toward the ORR could be increased. With a modified approach, the inactive iron present in OTf-Fe-OMC could possibly form active sites, thereby utilizing the higher solubility of the salt to generate a higher concentration of active sites and an improved catalytic performance for ORR.

■ ASSOCIATED CONTENT

Supporting Information

The Supporting Information is available free of charge on the ACS Publications website at DOI: 10.1021/acsomega.9b01803.

Details about elemental analysis and TGA, XRD, proton exchange membrane fuel cells, and rotating disc electrode (PDF)

■ AUTHOR INFORMATION

Corresponding Author

*E-mail: anders.palmqvist@chalmers.se.

ORCID

Samuel J. Fretz: 0000-0002-2288-1959

Caroline Janson: 0000-0002-2428-869X

Anders E. C. Palmqvist: 0000-0002-7579-3936

Author Contributions

†S.J.F. and C.J. authors contributed equally.

Notes

The authors declare no competing financial interest.

■ ACKNOWLEDGMENTS

The authors acknowledge funding support from The Swedish Energy Agency (Energimyndigheten) through project 38340-1. We thank Akzo Nobel for help with the XRF measurements. Part of this work was conducted at Chalmers Materials Analysis Laboratory (CMAL) with much help from Dr. Stefan Gustafsson.

■ REFERENCES

(1) Stein, A.; Wang, Z.; Fierke, M. A. Functionalization of Porous Carbon Materials with Designed Pore Architecture. *Adv. Mater.* **2009**, *21*, 265−293.

(2) Liang, C.; Li, Z.; Dai, S. Mesoporous carbon materials: synthesis and modification. *Angew. Chem., Int. Ed. Engl.* **2008**, *47*, 3696−3717.

(3) McCreery, R. L. Advanced carbon electrode materials for molecular electrochemistry. *Chem. Rev.* **2008**, *108*, 2646−2687.

(4) Benzigar, M. R.; Talapaneni, S. N.; Joseph, S.; Ramadass, K.; Singh, G.; Scaranto, J.; Ravon, U.; Al-Bahily, K.; Vinu, A. Recent advances in functionalized micro and mesoporous carbon materials: synthesis and applications. *Chem. Soc. Rev.* **2018**, *47*, 2680−2721.

(5) Kleitz, F.; Hei Choi, S.; Ryoo, R. Cubic Ia3d large mesoporous silica: synthesis and replication to platinum nanowires, carbon nanorods and carbon nanotubesElectronic supplementary information (ESI) available: TEM images of mesoporous cubic silica and Pt networks, XRD patterns during formation of the cubic phase. See http://www.rsc.org/suppdata/cc/b3/b306504a/. *Chem. Commun.* **2003**, 2136−2137.

(6) Li, R.; Ge, Y. J.; He, F.; Dou, L. T.; Liu, B. H.; Li, Z. P. Prevention of active-site destruction during the synthesis of high performance non-Pt cathode catalyst for fuel cells. *RSC Adv.* **2017**, *7*, 6622−6630.

(7) Pampel, J.; Fellinger, T. P. Opening of Bottleneck Pores for the Improvement of Nitrogen Doped Carbon Electrocatalysts. *Adv. Energy Mater.* **2016**, *6*, 1502389.

(8) Li, J.; Chen, J.; Wang, H.; Ren, Y.; Liu, K.; Tang, Y.; Shao, M. Fe/N co-doped carbon materials with controllable structure as highly efficient electrocatalysts for oxygen reduction reaction in Al-air batteries. *Energy Storage Mater.* **2017**, *8*, 49−58.

(9) Harris, P. J. F. New perspectives on the structure of graphitic carbons. *Crit. Rev. Solid State Mater. Sci.* **2005**, *30*, 235−253.

(10) Béguin, F.; Frackowiak, E. *Carbons for Electrochemical Energy Storage and Conversion Systems*; Tylor and Francis Group, 2009.

(11) Kinoshita, K. *Carbon: electrochemical and physicochemical properties*; Wiley: New York, 1988; p 533.

(12) Kiciński, W.; Szala, M.; Bystrzejewski, M. Sulfur-doped porous carbons: Synthesis and applications. *Carbon* **2014**, *68*, 1−32.

(13) Li, Z.; Yin, L. Nitrogen-doped MOF-derived micropores carbon as immobilizer for small sulfur molecules as a cathode for lithium sulfur batteries with excellent electrochemical performance. *ACS Appl. Mater. Interfaces* **2015**, *7*, 4029−4038.

(14) Paraknowitsch, J. P.; Thomas, A. Functional Carbon Materials From Ionic Liquid Precursors. *Macromol. Chem. Phys.* **2012**, *213*, 1132−1145.

(15) Shen, W.; Fan, W. Nitrogen-containing porous carbons: synthesis and application. *J. Mater. Chem. A* **2013**, *1*, 999−1013.

(16) Song, J.; Xu, T.; Gordin, M. L.; Zhu, P.; Lv, D.; Jiang, Y.-B.; Chen, Y.; Duan, Y.; Wang, D. Nitrogen-Doped Mesoporous Carbon Promoted Chemical Adsorption of Sulfur and Fabrication of High-Areal-Capacity Sulfur Cathode with Exceptional Cycling Stability for Lithium-Sulfur Batteries. *Adv. Funct. Mater.* **2014**, *24*, 1243−1250.

(17) Sun, F.; Wang, J.; Chen, H.; Li, W.; Qiao, W.; Long, D.; Ling, L. High efficiency immobilization of sulfur on nitrogen-enriched mesoporous carbons for Li-S batteries. *ACS Appl. Mater. Interfaces* **2013**, *5*, 5630−5638.

(18) Bo, X.; Guo, L. Ordered mesoporous boron-doped carbons as metal-free electrocatalysts for the oxygen reduction reaction in alkaline solution. *Phys. Chem. Chem. Phys.* **2013**, *15*, 2459−2465.

(19) Xia, L.; Zhong, B.; Zhang, T.; Hu, X.; Wu, S.; Yang, J.; Wen, G. Effect of boron doping on the thermal properties of carbon fibers reinforced lithium aluminosilicate matrix composites. *J. Eur. Ceram. Soc.* **2015**, *35*, 2555−2562.

DOI: 10.1021/acsomega.9b01803
ACS Omega 2019, 4, 17662−17671

(20) Xie, Y.; Meng, Z.; Cai, T.; Han, W.-Q. Effect of Boron-Doping on the Graphene Aerogel Used as Cathode for the Lithium-Sulfur Battery. *ACS Appl. Mater. Interfaces* **2015**, *7*, 25202−25210.
(21) Yang, C.-P.; Yin, Y.-X.; Ye, H.; Jiang, K.-C.; Zhang, J.; Guo, Y.-G. Insight into the effect of boron doping on sulfur/carbon cathode in lithium-sulfur batteries. *ACS Appl. Mater. Interfaces* **2014**, *6*, 8789−8795.
(22) Wang, H.-m.; Wang, H.-x.; Chen, Y.; Liu, Y.-j.; Zhao, J.-x.; Cai, Q.-h.; Wang, X.-z. Phosphorus-doped graphene and (8, 0) carbon nanotube: Structural, electronic, magnetic properties, and chemical reactivity. *Appl. Surf. Sci.* **2013**, *273*, 302−309.
(23) Yang, D.-S.; Bhattacharjya, D.; Inamdar, S.; Park, J.; Yu, J.-S. Phosphorus-doped ordered mesoporous carbons with different lengths as efficient metal-free electrocatalysts for oxygen reduction reaction in alkaline media. *J. Am. Chem. Soc.* **2012**, *134*, 16127−16130.
(24) Nitze, F.; Fossum, K.; Xiong, S.; Matic, A.; Palmqvist, A. E. C. Sulfur-doped ordered mesoporous carbons: A stability-improving sulfur host for lithium-sulfur battery cathodes. *J. Power Sources* **2016**, *317*, 112−119.
(25) See, K. A.; Jun, Y.-S.; Gerbec, J. A.; Sprafke, J. K.; Wudl, F.; Stucky, G. D.; Seshadri, R. Sulfur-functionalized mesoporous carbons as sulfur hosts in Li-S batteries: increasing the affinity of polysulfide intermediates to enhance performance. *ACS Appl. Mater. Interfaces* **2014**, *6*, 10908−10916.
(26) Ma, Z.-F.; Xie, X.-Y.; Ma, X.-X.; Zhang, D.-Y.; Ren, Q.; Hess-Mohr, N.; Schmidt, V. M. Electrochemical characteristics and performance of CoTMPP/BP oxygen reduction electrocatalysts for PEM fuel cell. *Electrochem. Commun.* **2006**, *8*, 389−394.
(27) Pylypenko, S.; Mukherjee, S.; Olson, T. S.; Atanassov, P. Non-platinum oxygen reduction electrocatalysts based on pyrolyzed transition metal macrocycles. *Electrochim. Acta* **2008**, *53*, 7875−7883.
(28) van Veen, J. A. R.; Vanbaar, J. F.; Kroese, C. J.; Coolegem, J. G. F.; Dewit, N.; Colijn, H. A. Oxygen Reduction on Transition-Metal Porphyrins in Acid Electrolyte .1. Activity. *Ber. Bunsen. Phys. Chem.* **1981**, *85*, 693−700.
(29) van Veen, J. A. R.; van Baar, J. F.; Kroese, K. J. Effect of heat treatment on the performance of carbon-supported transition-metal chelates in the electrochemical reduction of oxygen. *J. Chem. Soc., Faraday Trans. 1* **1981**, *77*, 2827−2843.
(30) Ziegelbauer, J. M.; Olson, T. S.; Pylypenko, S.; Alamgir, F.; Jaye, C.; Atanassov, P.; Mukerjee, S. Direct spectroscopic observation of the structural origin of peroxide generation from co-based pyrolyzed porphyrins for ORR applications. *J. Phys. Chem. C* **2008**, *112*, 8839−8849.
(31) Faubert, G.; Lalande, G.; Côté, R.; Guay, D.; Dodelet, J. P.; Weng, L. T.; Bertrand, P.; Dénès, G. Heat-treated iron and cobalt tetraphenylporphyrins adsorbed on carbon black: Physical characterization and catalytic properties of these materials for the reduction of oxygen in polymer electrolyte fuel cells. *Electrochim. Acta* **1996**, *41*, 1689−1701.
(32) van Veen, J. A. R.; Visser, C. Oxygen reduction on monomeric transition metal phthalocyanines in acid electrolyte. *Electrochim. Acta* **1979**, *24*, 921−928.
(33) Wiesener, K.; Ohms, D.; Neumann, V.; Franke, R. N4 macrocycles as electrocatalysts for the cathodic reduction of oxygen. *Mater. Chem. Phys.* **1989**, *22*, 457−475.
(34) Bron, M.; Radnik, J.; Fieber-Erdmann, M.; Bogdanoff, P.; Fiechter, S. EXAFS, XPS and electrochemical studies on oxygen reduction catalysts obtained by heat treatment of iron phenanthroline complexes supported on high surface area carbon black. *J. Electroanal. Chem.* **2002**, *535*, 113−119.
(35) Lefèvre, M.; Proietti, E.; Jaouen, F.; Dodelet, J.-P. Iron-based catalysts with improved oxygen reduction activity in polymer electrolyte fuel cells. *Science* **2009**, *324*, 71−74.
(36) Dombrovskis, J. K.; Jeong, H. Y.; Fossum, K.; Terasaki, O.; Palmqvist, A. E. C. Transition Metal Ion-Chelating Ordered Mesoporous Carbons as Noble Metal-Free Fuel Cell Catalysts. *Chem. Mater.* **2013**, *25*, 856−861.
(37) Dombrovskis, J. K.; Palmqvist, A. E. C. The Active Site Structure of Transition Metal Ion-Chelating Ordered Mesoporous Carbon Fuel Cell Catalysts. *Fuel Cells* **2016**, *16*, 23−31.
(38) Dombrovskis, J. K.; Palmqvist, A. E. C. Recent Progress in Synthesis, Characterization and Evaluation of Non-Precious Metal Catalysts for the Oxygen Reduction Reaction. *Fuel Cells* **2016**, *16*, 4−22.
(39) Janson, C.; Palmqvist, A. E. C. Influence of Precursor Functional Groups on the Formation and Performance of Iron-Coordinating Ordered Mesoporous Carbons as Fuel Cell Catalysts. *J. Phys. Chem. C* **2017**, *121*, 21827−21835.
(40) Liu, D.; Fu, L.; Huang, X.; Liu, K.; Li, J.; Xie, H.; Wang, H.; Tang, Y. Influence of Iron Source Type on the Electrocatalytic Activity toward Oxygen Reduction Reaction in Fe-N/C for Al-Air Batteries. *J. Electrochem. Soc.* **2018**, *165*, F662−F670.
(41) Dombrovskis, J. K.; Prestel, C.; Palmqvist, A. E. C. Optimization of fuel cell membrane electrode assemblies for transition metal ion-chelating ordered mesoporous carbon cathode catalysts. *Apl. Mater.* **2014**, *2*, 121102.
(42) Janson, C.; Dombrovskis, J. K.; Palmqvist, A. E. C. Influence of iron precursor hydration state on performance of non-precious metal fuel cell catalysts. *J. Mater. Chem. A* **2018**, *6*, 3116−3125.
(43) Dombrovskis, J. K.; Palmqvist, A. E. C. One-pot synthesis of transition metal ion-chelating ordered mesoporous carbon/carbon nanotube composites for active and durable fuel cell catalysts. *J. Power Sources* **2017**, *357*, 87−96.
(44) Ramaswamy, N.; Tylus, U.; Jia, Q.; Mukerjee, S. Activity descriptor identification for oxygen reduction on nonprecious electrocatalysts: linking surface science to coordination chemistry. *J. Am. Chem. Soc.* **2013**, *135*, 15443−15449.
(45) Ge, X.; Sumboja, A.; Wuu, D.; An, T.; Li, B.; Goh, F. W. T.; Hor, T. S. A.; Zong, Y.; Liu, Z. Oxygen Reduction in Alkaline Media: From Mechanisms to Recent Advances of Catalysts. *ACS Catal.* **2015**, *5*, 4643−4667.
(46) Janson, C.; Palmqvist, A. E. C., Electron Paramagnetic Resonance Spectroscopy Analysis of Iron-Chelating Ordered Mesoporous Carbons for Oxygen Reduction Fuel Cell Catalysts. *Commun. Chem.*, under revision.
(47) Burstyn, J. N.; Roe, J. A.; Miksztal, A. R.; Shaevitz, B. A.; Lang, G.; Valentine, J. S. Magnetic and spectroscopic characterization of an iron porphyrin peroxide complex. Peroxoferrioctaethylporphyrin(1-). *J. Am. Chem. Soc.* **1988**, *110*, 1382−1388.
(48) Yatsunyk, L. A.; Walker, F. A. NMR and EPR spectroscopic and structural studies of low-spin, $(d_{xz},d_{yz})^4(d_{xy})^1$ ground state Fe(III) bis-tert-butylisocyanide complexes of dodecasubstituted porphyrins. *Inorg. Chem.* **2004**, *43*, 4341−4352.
(49) Petasis, D. T.; Hendrich, M. P. Quantitative interpretation of EPR spectroscopy with applications for iron-sulfur proteins. In *Iron-Sulfur Clusters in Chemistry and Biology*, Rouault, T. A., Ed.; De Gruyter, 2014; pp 21-48.
(50) Wittenberg, J. B.; Wittenberg, B. A.; Peisach, J.; Blumberg, W. E. On the state of the iron and the nature of the ligand in oxyhemoglobin. *Proc. Natl. Acad. Sci. U.S.A.* **1970**, *67*, 1846−1853.
(51) Lan, M.; Zhao, H.; Yuan, H.; Jiang, C.; Zuo, S.; Jiang, Y. Absorption and EPR spectra of some porphyrins and metalloporphyrins. *Dyes Pigments* **2007**, *74*, 357−362.
(52) Shpak, A.; Kolesnik, S.; Mogilny, G.; Petrov, Y.; Sokhatsky, V.; Trophimova, L.; Shanina, B.; Gavriljuk, V. Structure and magnetic properties of iron nanowires encased in multiwalled carbon nanotubes. *Acta Mater.* **2007**, *55*, 1769−1778.
(53) Koksharov, Y. A.; Pankratov, D. A.; Gubin, S. P.; Kosobudsky, I. D.; Beltran, M.; Khodorkovsky, Y.; Tishin, A. M. Electron paramagnetic resonance of ferrite nanoparticles. *J. Appl. Phys.* **2001**, *89*, 2293−2298.
(54) Ferguson, R. M.; Minard, K. R.; Krishnan, K. M. Optimization of nanoparticle core size for magnetic particle imaging. *J. Magn. Magn. Mater.* **2009**, *321*, 1548−1551.
(55) van der Kraan, A. M.; Ramselaar, W. L. T. M.; de Beer, V. H. J. Mössbauer Spectroscopy of Iron and Iron-Molybdenum Hydro-

DOI: 10.1021/acsomega.9b01803
ACS Omega 2019, 4, 17662−17671

treating Catalysts. In *Mössbauer Spectroscopy Applied to Inorganic Chemistry*; Long, G. J., Grandjean, F., Eds.; Springer: Boston, MA, USA, 1989; Vol. 3.
(56) Takayama, T.; Takagi, H. Phase-change magnetic memory effect in cation-deficient iron sulfide $Fe_{1-x}S$. *Appl. Phys. Lett.* **2006**, *88*, 012512.

DOI: 10.1021/acsomega.9b01803
ACS Omega 2019, 4, 17662−17671